UC Irvine
UC Irvine Previously Published Works

Title
Optical and acoustic scattering in cutaneous neurofibromas: Implications for early detection

Permalink
https://escholarship.org/uc/item/3rw9605z

Journal
Journal of Investigative Dermatology, 146(9)

ISSN
0022-202X

Authors
Jia, Wangcun
Katta, Nitesh
Kennedy, Gordon T
et al.

Publication Date
2026-09-01

DOI
10.1016/j.jid.2026.02.015

Copyright Information
This work is made available under the terms of a Creative Commons Attribution License, available at https://creativecommons.org/licenses/by/4.0/

Peer reviewed

eScholarship.org Powered by the California Digital Library
University of California

Optical and acoustic scattering in cutaneous neurofibromas: Implications for early detection

Wangcun Jia[1], Nitesh Katta[1,2], Gordon T. Kennedy[1], Junsoo Lee[1,2], Emily Nguyen[1], Oswald Lai[1], Yurie Jeong[1], Rachel Elsanadi[3], Feben Messele[3], James E. Johnson[2], Anat O. Stemmer-Rachamimov[4,5], J. Stuart Nelson[1], Rafael Sierra[6], Kristen M. Kelly[1,3], Anthony J. Durkin[1,7] and Thomas E. Milner[2]

Journal of Investigative Dermatology (2026) **146,** 2530–2540; doi:10.1016/j.jid.2026.02.015

Cutaneous neurofibromas (cNFs) occur in individuals with germline neurofibromatosis type I pathogenic variants. Current management involves monitoring and limited surgical removal. Nascent cNFs are lesions detectable only through advanced imaging and not observable with the unaided eye. Noninvasive early detection may enable intervention before cNF become visible. We introduce an imaging approach integrating spatial frequency domain imaging and high-frequency ultrasound to identify and characterize suspected nascent cNFs. In 21 participants with neurofibromatosis type I, we identified 152 suspected nascent lesions using spatial frequency domain imaging as skin regions with decreased optical scattering at near-infrared wavelengths. Of these, 120 were imaged with high-frequency ultrasound, and 93% demonstrated subsurface hypoechoic dermal structures. Paired analyses of the reduced scattering coefficient (μ_s') at 851 nm showed that μ_s' within suspected nascent cNFs was significantly lower than that of adjacent uninvolved skin, supporting μ_s' as a candidate imaging feature for nascent cNFs. Statistical variation in overlying dermal thickness and lesion dimensions is summarized. Integrating spatial frequency domain imaging and high-frequency ultrasound represents a multimodal approach for imaging characterization of suspected nascent cNFs and may advance the understanding of cNF progression and the development of treatment strategies. This feasibility study does not establish nascent cNF diagnostic detection accuracy because histologic confirmation was limited.

Keywords: Cutaneous neurofibromas, High-frequency ultrasound, Spatial frequency domain imaging

INTRODUCTION

Neurofibromatosis type I (NF1) is a neurogenetic disorder that occurs in approximately 1 in 3000 individuals (Friedman, 1999; Huson et al, 1988; Kallionpää et al, 2018). Cutaneous neurofibromas (cNFs) are lesions in the skin that impact most individuals with NF1. cNFs can appear in individuals as young as 6 years old (Huson et al, 1988) but grow more rapidly around puberty, increasing in both number and size. Despite being benign, cNF lesions, which can number up to thousands, can disfigure the body, including the neck and face (Ehara et al, 2018). Visible cNFs that protrude above the skin can cause psychological distress, social isolation, and physical discomfort, impacting QOL and emotional well-being (Kodra et al, 2009; Page et al, 2006; Wolkenstein et al, 2001).

cNFs arise in individuals who carry germline NF1 variants and subsequently acquire a second somatic hit in the NF1 gene in tumor cells, leading to biallelic NF1 inactivation, loss of neurofibromin, and constitutive Ras pathway activation (Maertens et al, 2006; Serra et al, 1997). These molecular events drive uncontrolled cell growth and the formation of neurofibromas (Muir et al, 2001). cNFs are complex structures found within the dermis, consisting of a variety of cellular constituents, including Schwann cells, fibroblasts, macrophages, and mast cells, all embedded in a collagen-rich matrix (Jouhilahti et al, 2011; Peltonen et al, 1988). The number and size of cNFs can vary greatly and manifest in various forms (Duong et al, 2011; Easton et al, 1993). The initial, nascent form is detected only through advanced imaging modalities (Chamseddin et al, 2019) and is usually invisible or difficult to detect with the unaided eye. When cNFs progress beyond the imperceptible nascent stage and emerge from the dermis to become visible, patient well-being and QOL are impacted.

The clinical management of cNF involves monitoring smaller lesions and surgically removing larger, protruding tumors when they cause physical and/or psychological distress for patients. Regrettably, the surgical removal of cNF cannot completely restore patients' QOL. Significant morbidity, most notably postsurgical scarring and tumor recurrence, is problematic (Bromley et al, 1982; Kim et al,

[1]Beckman Laser Institute, University of California, Irvine, Irvine, California, USA; [2]Michael E. DeBakey Center for Nano-Biophotonics, Baylor College of Medicine, Houston, Texas, USA; [3]Department of Dermatology, University of California, Irvine, Irvine, California, USA; [4]Department of Pathology, Massachusetts General Hospital and Harvard Medical School, Boston, Massachusetts, USA; [5]Center for Cancer Research, Massachusetts General Hospital and Harvard Medical School, Boston, Massachusetts, USA; [6]Medical Laser Consultant, Gulf Port, Florida, USA; and [7]Department of Biomedical Engineering, University of California, Irvine, Irvine, California, USA

Correspondence: Thomas E. Milner, Michael E. DeBakey Center for Nano-Biophotonics, Baylor College of Medicine, 1 Baylor Plaza, Houston, Texas 77030, USA. E-mail: Thomas.Milner@bcm.edu

Abbreviations: CI, confidence interval; cNF, cutaneous neurofibroma; HFUS, high-frequency ultrasound; NF1, neurofibromatosis type I; SFDI, spatial frequency domain imaging; sn_cNF, suspected nascent cutaneous neurofibroma

Received 26 June 2025; revised 10 February 2026; accepted 13 February 2026; accepted manuscript published online 6 March 2026; corrected proof published online 17 April 2026

© 2026 Published by Elsevier Inc. on behalf of Society for Investigative Dermatology.

2012; Lutterodt et al, 2016; Méni et al, 2015; Roenigk and Ratz, 1987). No treatments are currently available that prevent the initiation of cNFs or inhibit their progression. The lack of wide-field detection of nascent cNFs, together with the absence of preventive and proactive therapeutic options, presents a significant challenge and a critical gap in the clinical management of cNF.

To address this gap, clinical management may benefit from specialized wide-field imaging instrumentation that can rapidly screen large skin areas and identify suspected lesions that are otherwise invisible to the unaided eye. cNFs can manifest at any anatomical site, with higher numbers on the trunk and fewer lesions on the lower limbs (Ehara et al, 2018). Consequently, candidate imaging instrumentation should offer a wide field of view to facilitate rapid full-body screening during a single office visit. Moreover, owing to the diminutive size of early-stage cNF lesions, candidate imaging instrumentation must provide a spatial resolution of at least 0.5−1 mm. In a preliminary study, we demonstrated the potential of spatial frequency domain imaging (SFDI) as an effective approach for scanning large-sized skin areas to identify invisible cNF in a limited number of subjects (Li et al, 2023).

SFDI is a wide-field, noncontact imaging modality, developed at the Beckman Laser Institute and Medical Clinic (Cuccia et al, 2005). SFDI is based on diffuse optical spectroscopy and is well-suited for quantitative large field-of-view in vivo imaging to detect skin lesions (Durkin et al, 2008; Konecky et al, 2009; Mazhar et al, 2012; Nguyen et al, 2013; Phan et al, 2021; Ponticorvo et al, 2013). SFDI provides spatially resolved maps of tissue optical properties, including optical scattering and absorption coefficients. Owing to its unique capabilities to provide quantitative physiological and molecular tissue information, combined with its relative simplicity and safety, SFDI has attracted increased interest in biomedical imaging research (Gioux et al, 2019; Kennedy et al, 2019; Lee et al, 2020; Saidian et al, 2019).

In this study, we used SFDI to examine the skin of 21 patients with NF1. From SFDI-derived optical scattering maps at various wavelengths, we identified clinically normal-appearing regions with decreased optical scattering at near-infrared wavelengths relative to adjacent skin, which we hypothesized to represent nascent cNF. To further characterize these suspected lesions, we performed high-frequency ultrasound (HFUS) imaging, which revealed subsurface hypoechoic regions in the suspected lesions, providing complementary structural characterization and aligning with prior reports that cNFs exhibit decreased acoustic scattering in HFUS images (García-Martínez et al, 2023; Oteiza-Rius et al, 2025; Raffin et al, 2017; Zarchi et al, 2014). In a small subset of lesions, biopsy and histopathology confirmed the presence of cNF. Inasmuch as longitudinal observation of suspected cNF is a primary endpoint of this study, most suspected cNFs were not biopsied. Accordingly, the data presented here are not sufficient to establish diagnostic accuracy, sensitivity, or specificity of nascent cNF identification using either SFDI or HFUS. In the work reported here, skin regions that present both decreased optical and acoustic scattering in patients with NF1 and are not readily visible to the unaided eye are referred to as "suspected nascent cNF (sn_cNF)." The objective of the study is to evaluate the feasibility of using the reduced scattering coefficient (μ_s') measured by SFDI at near infrared wavelengths as a candidate imaging feature for sn_cNF detection and assess agreement with HFUS.

RESULTS

Subject demographics

Twenty-one research participants with diagnosed NF1 were enrolled in the study (Table 1). The participants' ages varied from 11 to 62 years. The median age of 23 falls within the younger demographic, with a notable portion of subjects being adolescents (aged <18 years, 43%). Subject age distribution reflects an intentional recruitment of younger participants to image early stage cNF lesions. The study included 13 males (62%) and 8 females (38%). Males were younger on average than females (mean age of 24.3 vs 33.9 years, $P = .226$). Fitzpatrick skin types were distributed as follows: 4 of 21 (19.0%) for type I, 6 of 21 (28.6%) for type II, 5 of 21 (23.8%) for type III, 5 of 21 (23.8%) for type IV, and 1 of 21 (4.8%) for type V. We aimed to recruit across all Fitzpatrick skin types; however, no type VI participants were successfully enrolled.

Characterizing optical and acoustic scattering anomalies as potential cNF indicators across age-stratified patients with NF1

Table 1 summarizes, for each subject, the number of sn_cNFs identified from SFDI-derived μ_s' maps on the chest, back, and left arm. For the chest and back, the table also reports the mean μ_s' at 851 nm wavelength within sn_cNF (μ_{s_SN}') and the mean μ_s' within adjacent uninvolved skin (μ_{s_U}') for each subject. In the remaining parts of this paper, μ_s' refers to μ_s' at 851 nm. Mean μ_s' values for the left arm are provided in supplementary Table S1 owing to the limited number of sn_cNFs at that site. No sn_cNF was observed on the right arm. For each subject and body site, the number of sn_cNFs exhibiting hypoechoicity in HFUS is also reported. When no sn_cNFs were detected at a site, HFUS was not performed, and the corresponding entries are designated as "NA."

On the basis of observed imaging characteristics and lesion distributions across the cohort, subjects were stratified post-hoc into 3 descriptive groups to facilitate presentation of results. This stratification reflected patterns observed in age, lesion burden, and the visual separation between suspected nascent and more developed cNFs on imaging. The resulting groups corresponded broadly to younger (10−19 years), intermediate (20−49 years), and older (≥50 years) subjects and are used in this study solely as an organizational framework for summarizing imaging features and trends.

Group I. This group includes 10 subjects aged 10−19 years (green-shaded cells in the age column of Table 1). In this group, sn_cNFs were visually well-separated from surrounding skin and from more developed lesions on SFDI and HFUS imaging.

Across chest and back sites, μ_{s_SN}' was consistently lower than μ_{s_U}', with large within-subject effect sizes and highly significant paired differences (Supplementary Table S2). HFUS confirmation conditional on μ_s' positivity was high

Table 1. Subject Demographics and Suspected Nascent cNF Characteristics

Nascent cNF				Suspected Nascent cNF								Total	
Subject ID	Age, y	Sex	Skin Type	Chest	μ_s', SN/U[1]	Hypo echoic	Back	μ_s', SN/U[1]	Hypo echoic	Left arm	Hypo echoic	Lower m_s'	Hypo echoic
3	11	F	III	4	1.21/1.44	3	6	1.30/1.52	5	0	NA	10	8
19	12	M	III	2	1.23/1.49	2	9	1.34/1.47	4	0	NA	11	6
17	13	M	I	3	1.30/1.63	3	7	1.42/1.58	7	0	NA	10	10
7	14	M	II	2	1.39/1.71	2	2	1.35/1.58	2	1	1	5	5
20	14	M	III	6	1.53/1.66	6	3	1.37/1.55	3	0	NA	9	9
8	15	M	III	0	/1.65	NA	0	/1.52	NA	0	NA	0	0
11	15	M	IV	2	1.48/1.62	2	0	/1.65	0	0	NA	2	2
9	17	M	IV	5	1.08/1.38	5	3	1.11/1.37	3	0	NA	8	8
10	17	M	II	0	/1.90	NA	0	/1.77	NA	0	NA	0	0
6	18	F	I	2	1.19/1.37	2	3	1.11/1.32	3	0	NA	5	5
21	23	F	III	3	1.03/1.19	2	0	/1.19	NA	2	2	5	4
12	24	M	I	11	1.35/1.50	11	6	1.21/1.40	6	0	NA	17	17
13	29	M	I	0	/1.60	NA	0	/1.67	NA	0	NA	0	0
18	30	F	II	0	/1.20	NA	0	/1.18	NA	0	NA	0	0
5	35	M	IV	4	1.19/1.43	4	6	1.15/1.36	6	0	NA	10	10
15	35	F	IV	0	/1.25	NA	6	1.16/1.31	3	1	1	7	4 of 4
16	37	F	IV	14	1.07/1.2	3	20	1.21/1.31	6	0	NA	34	9 of 9
1	55	F	II	0	/1.19	NA	5	1.03/1.21	5	0	NA	5	5
4	55	M	II	2	1.0/1.3	2	0	/1.38	NA	0	NA	2	2
2	56	M	II	5	1.0/1.23	5	7	1.07/1.25	7	0	NA	12	12
14	62	F	V	0	/1.38	NA	0	/1.26	NA	0	NA	0	0

Abbreviations: cNF, cutaneous neurofibroma; F, female; HFUS, high-frequency ultrasound; ID, identification; M, male; NA, not available.
[1]m_s' denotes reduced scattering coefficient at 851 nm wavelength, mm^{-1}; SN denotes suspected nascent cNF; U denotes adjacent uninvolved skin, and NA denotes HFUS imaging not performed.

overall, with stronger agreement on the chest than on the back.

Group II. This group comprised 7 subjects aged 20–49 years (orange-shaded cells in the age column of Table 1). Compared with group I, greater overlap in imaging appearance was observed between sn_cNFs and more developed cNFs, reflecting increased phenotypic heterogeneity.

Despite this overlap, $\mu_s'_{SN}$ remained consistently lower than $\mu_s'_{U}$ across chest and back sites, with large within-subject effect sizes and statistically significant paired differences (Supplementary Table S2). HFUS confirmation rates were high for both chest and back, yielding near-complete agreement in this group.

Group III. This group includes 4 subjects aged >50 years (red-shaded cells in the age column of Table 1). Subjects in this group exhibited a high overall burden of cNFs, with frequent spatial clustering of lesions at different stages and substantial overlap in imaging appearance between suspected nascent and more developed cNFs. Nevertheless, SFDI scattering maps provided substantially greater lesion contrast than conventional color images.

Across chest and back sites, $\mu_s'_{SN}$ was again lower than $\mu_s'_{U}$, with large pooled effect sizes despite small sample sizes and wider confidence intervals (CIs) (Supplementary Table S2). HFUS confirmation conditional on μ_s' positivity was complete in this group.

The representative multimodal imaging results for groups I, II, and III are presented as follows. Figure 1 illustrates the nuanced identification of sn_cNF. Figure 1a displays a color image of the patient's chest and highlights the limitation of conventional imaging for identifying nascent cNFs. In Figure 1b, the SFDI μ_s' map of the same anatomical region reveals darker regions with μ_s' values lower than surrounding skin that are postulated to align with nascent cNFs. The hypothesis that correlates sn_cNF with SFDI regions with low μ_s' gains further support from HFUS images depicted in Figure 1c. HFUS reveals corresponding hypoechoic structures within the dermis, consistent with subclinical lesion formation. The presence of hypoechoic regions suggests a distinctive tissue microstructure, possibly owing to the development of cNF, even at the nascent stage that is invisible to the unaided eye or traditional imaging methods. The multimodal imaging approach utilized in this study, including SFDI scattering maps and HFUS images, demonstrates feasibility for imaging characterization of sn_cNFs in younger patients (group I), although histologic confirmation is needed to validate these findings.

Figure 2 presents multimodal imaging results from the chest area of a female patient with NF1 aged 37 years (group II). In the color image of the chest (Figure 2a), multiple cNF lesions are observed and appear as small, raised bumps alongside numerous darker-colored macules. The subsequent Figure 2b presents the SFDI μ_s' map of the same area revealing regions of lower μ_s' than surrounding skin. Both suspected nascent (yellow outline) and more developed cNFs share the characteristic of lower μ_s', indicating an important shared optical property at different stages of lesion development. Figure 2c illustrates evolution of cNF development, from the earliest, nascent stage to more developed forms such

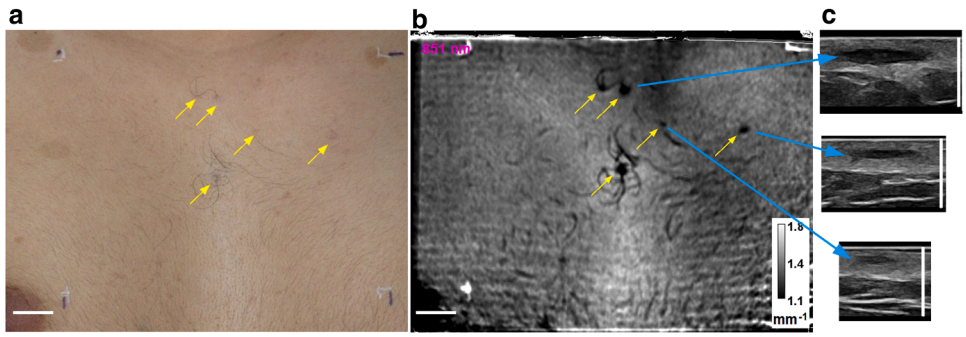

Figure 1. Representative multimodal imaging results of sn_cNF in group I subjects (aged 10–19 years). (**a**) Color image of the chest (male subject aged 17 years). cNF lesions are not readily visible, illustrating the limitation of conventional color imaging for identifying nascent cNF. (**b**) SFDI μ_s' maps at 851 nm wavelength of the same region; darker areas (yellow arrows) indicate lower μ_s' than adjacent skin and are identified as candidate sn_cNF. (**c**) HFUS images of the candidate sn_cNF show hypoechoic structures within the dermis (blue arrows), supporting the presence of subclinical lesions. Horizontal bar = 20 mm; vertical bar = 5 mm. cNF, cutaneous neurofibroma; HFUS, high-frequency ultrasound; SFDI, spatial frequency domain imaging; sn_cNF**,** suspected nascent cutaneous neurofibroma.

as flat, sessile, globular, and peduncular cNFs (Chamseddin et al, 2019); all of these stages are observed in this patient. The corresponding HFUS images in Figure 2d show dermal involvement in suspected nascent and flat lesion stages. Similar to group I, these images display hypoechoic structure within the dermis, consistent with altered tissue microstructure associated with cNFs. All stages of cNF development are captured in Figure 2, combining optical and ultrasound diagnostic techniques to highlight lesion stage and progression.

Figure 3 illustrates representative multimodal imaging results of a subject in group III. Figure 3a shows a color photograph of the skin, revealing numerous scattered cNFs. Figure 3b is an SFDI μ_s' map that provides higher cNF contrast than the color image. Figure 3c shows cNF locations (yellow outlines) delineated using a threshold-based segmentation algorithm applied to the SFDI scattering map. The cNF image segmentation may prove useful for tracking lesion progression and potentially facilitate therapeutic planning, offering a pathway toward more personalized and precise interventions. Collectively, these results indicate that SFDI scattering maps provide enhanced contrast for delineating cNFs in subjects with high lesion burden.

Age, lesion burden, and HFUS concordance analysis and characterization

Across stratified analyses, a consistent within-subject reduction in $\mu_s'_{_SN}$ relative to $\mu_s'_{_U}$ was observed, with large effect sizes despite modest sample sizes in some strata (Supplementary Table S2). Both $\mu_s'_{_SN}$ and $\mu_s'_{_U}$ exhibited gradual declines with age (0.07–0.08 mm^{-1} per decade), whereas the within-subject contrast ($\Delta\mu_s'$) remained comparatively stable across the age range studied.

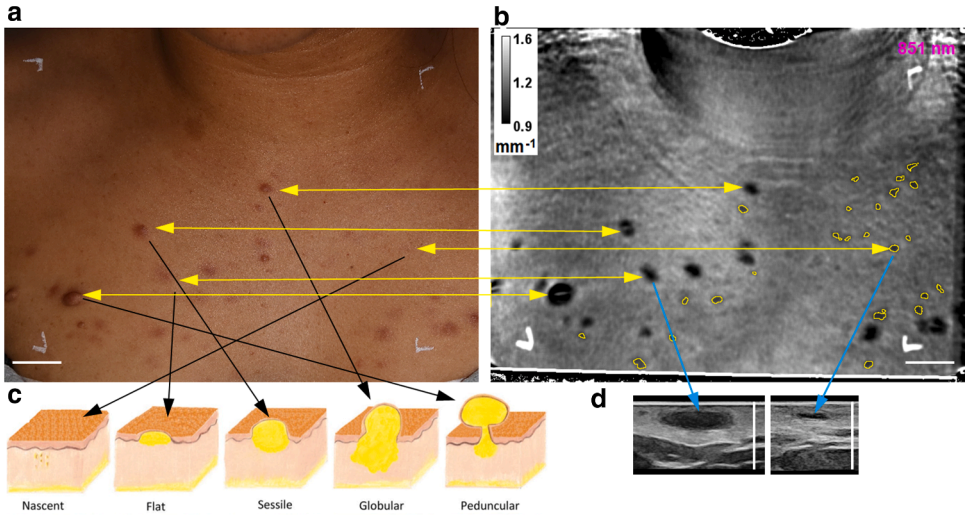

Figure 2. Representative multimodal imaging results of sn_cNF in group II subjects (aged 20–49 years). **(a)** Color photograph of the chest of a female patient with NF1 aged 37 years, showing multiple raised cNF lesions and pigmented macules. (**b**) SFDI μ_s' maps of the same area at 851 nm wavelength, in which regions of lower μ_s' than adjacent skin are observed in both developed cNF and candidate sn_cNF (yellow outlines). sn_cNFs are barely visible in the color image. (**c**) Illustration of different stages of cNF (Chamseddin et al, 2019), all of which are present in this patient. Image was adapted with permission from American Society for Clinical Investigation. (**d**) HFUS images of a developed and an sn_cNF showing hypoechoic structures within dermis. Horizontal bar = 20 mm; vertical bar = 5 mm. cNF, cutaneous neurofibroma; HFUS, high-frequency ultrasound; NF1, neurofibromatosis type I; SFDI, spatial frequency domain imaging; sn_cNF**,** suspected nascent cutaneous neurofibroma.

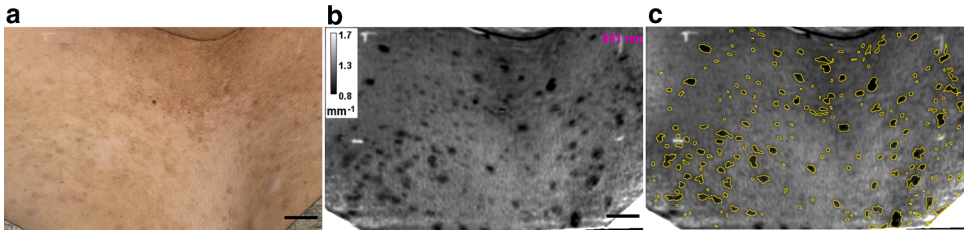

Figure 3. Representative multimodal imaging results of cNF in group III subjects (aged >50 years). **(a)** Color photograph of the chest of a female aged 55 years showing numerous scattered cNF. (**b**) SFDI μ_s' map at 851 nm wavelength, in which cNFs are depicted with higher contrast than the color image. (**c**) Locations of cNFs highlighted with yellow outlines using a threshold-based segmentation algorithm applied to the SFDI scattering map. Bar = 20 mm. cNF, cutaneous neurofibroma; SFDI, spatial frequency domain imaging.

Differences by sex were small after considering age, and no reproducible ordered pattern was observed with Fitzpatrick skin type. Given modest subgroup sizes and uneven age distributions across categories, these results should be interpreted cautiously.

Lesion burden was not strongly associated with μ_s'. Spearman correlations between the number of sn_cNF and μ_{s_SN}' or $\Delta\mu_s'$ were weak, indicating that within the observed range, lesion burden was not a primary determinant of scattering magnitude or contrast.

Counts of sn_cNFs and developed cNFs varied substantially across subjects and age groups, with no consistent monotonic relationship with age (Supplementary Table S1). The number of developed cNFs does not appear to correlate directly with the number of detected sn_cNF because some groups showing more sn_cNF but fewer developed or vice versa.

In all 3 groups, HFUS confirmation conditional on μ_s' positivity was high. Overall confirmation rates were 0.96 on the chest and 0.91 on the back, yielding a pooled rate of 0.93 (Supplementary Table S3). Although confirmation appeared lower on the back than on the chest, between-site differences were not statistically significant and were accompanied by wide CIs. At the subject level, agreement between SFDI-identified candidate sn_cNF counts and HFUS-confirmed lesion counts was further assessed using Bland–Altman analysis and concordance correlation coefficients (Supplementary Table S4). Agreement was high on the chest, with minimal bias and narrow limits of agreement, whereas agreement on the back remained strong but exhibited greater variability, driven primarily by a small number of subjects with partial HFUS confirmation.

HFUS revealed substantial variability in sn_cNF morphology across lesions. Representative HFUS images illustrating this heterogeneity are shown in Supplementary Figure S1, including examples of a thin, flat sn_cNF and a barely visible cNF that is considerably wider and thicker. Quantitative summaries of cNF spatial dimensions derived from HFUS cross-sectional images for groups I–III are presented in Figure 4, with group-level descriptive statistics summarized in Supplementary Table S4 and subject-level geometry provided in Supplementary Figures S2–S5. Among measured dimensions, only mean lesion thickness increased monotonically across age groups, with a statistically significant overall group effect with small effect sizes. Pairwise differences did not remain significant after correction, with the largest difference observed between group I and group III, consistent with a trend toward thicker lesions in older subjects. Statistical analyses of lesion thickness across age groups are reported in Supplementary Tables S5 and S6.

Histologic analysis of nascent cNFs

When a biopsy was taken, visible and sn_cNFs could be positively identified by a dermatopathologist (coauthor, AOS-R). In Figure 5a, biopsy sites are marked with red, yellow, and black circles, indicating a sessile cNF, an sn_cNF, and adjacent uninvolved skin, respectively. The color photo and SFDI scattering map (Figure 5a and b) demonstrate that the sessile cNF is visible in both imaging modalities, whereas the sn_cNF is apparent only in the SFDI scattering map, highlighting the ability of SFDI to detect nascent lesions. Histologic sections in Figure 5c and d further elucidate these findings; the nascent cNF shows a lesion composed of spindled cells and an altered basophilic matrix, indicating significant changes in cellular and stromal components, whereas the uninvolved skin is less cellular and more eosinophilic. The differences in staining and cellularity between the 2 sections highlight the lack of cellular proliferation in the uninvolved skin, which is a key indicator in distinguishing uninvolved skin from the cNF (Jouhilahti et al, 2011; Nagrani and Bhawan, 2022).

DISCUSSION

Within subjects, reduced scattering coefficient (μ_s') at 851 nm (referred to as μ_s' in the remaining parts of this paper) was substantially and consistently lower in sn_cNF than in adjacent uninvolved skin regions, with large and precise effects at both body sites. These findings support the utility of μ_s' as an imaging contrast for in vivo identification of sn_cNF. The modeling of the within-subject contrast, $\Delta\mu_s' = \mu_{s_SN}' - \mu_{s_U}'$, against age showed that although both μ_{s_SN}' and μ_{s_U}' tend to decrease with age, $\Delta\mu_s'$ remained relatively stable across ages in this cohort. The result implies that the contrast provided by $\Delta\mu_s'$ between suspected lesions and surrounding skin is not strongly age dependent within the studied range, which may be advantageous for longitudinal imaging applications.

Lesion burden, quantified as the count of sn_cNF on a site, did not correlate meaningfully with either the absolute μ_s' within sn_cNF or the contrast $\Delta\mu_s'$. The absence of a trend suggests that lesion-level mean μ_s' and its contrast to adjacent skin are not simply driven by the number of lesions present but more likely by local tissue microstructure and composition. This observation aligns with a mechanistic view in

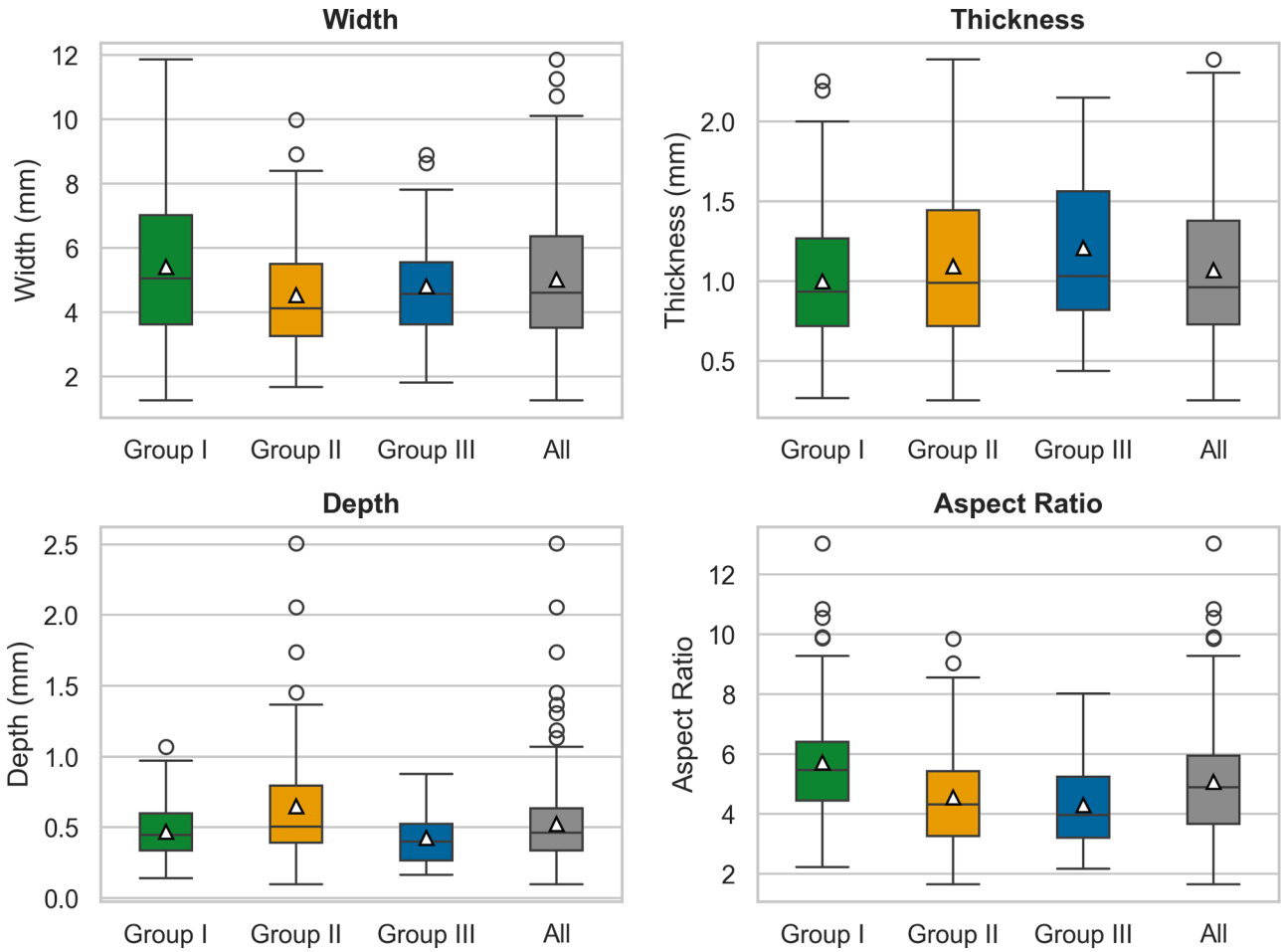

Figure 4. Morphological characteristics of sn_cNF derived from HFUS cross-sectional images in groups I, II, and III. Definition of width, thickness, and depth can be found in Supplementary Figure S8. A table of the values can be found in Supplementary Table S4. cNF, cutaneous neurofibroma; HFUS, high-frequency ultrasound; sn_cNF, suspected nascent cutaneous neurofibroma.

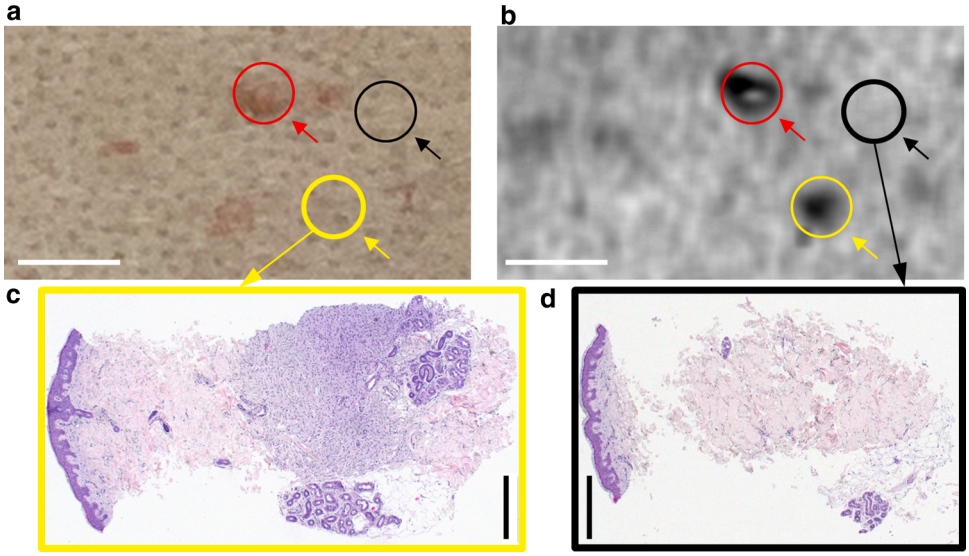

Figure 5. Photo, SFDI scattering map, and histological sections of a sessile and a sn_cNF. (**a, b**) Locations of biopsy sites. Red circle: a sessile cNF; yellow circle: an sn_cNF; black circle: uninvolved skin area. (**c**) Nascent cNF, characterized by increased cellularity and basophilic staining, indicating change in cellular and stromal composition. (**d**) Adjacent uninvolved skin, which is eosinophilic and less compact, indicating a lack of the same cellular proliferation seen in the nascent cNF. Horizontal bar = 10 mm; vertical bar = 0.5 mm. cNF, cutaneous neurofibroma; SFDI, spatial frequency domain imaging; sn_cNF, suspected nascent cutaneous neurofibroma.

which μ_s' reflects scattering properties within the lesion rather than a load-dependent effect at the site level.

In this verification design, HFUS hypoechoic signal confirmed the substantial majority of sites flagged by decreased μ_s', with confirmation rates of approximately 96% on the chest and 91% on the back, and an overall rate of 93%. Although the point estimate suggested lower confirmation on the back, the statistical comparison did not demonstrate a significant difference, and the CI was wide, consistent with limited power and between-subject variability. Subject-level summaries and Bland–Altman analysis showed close agreement for most individuals, with a small number of partial confirmations (particularly one subject's back with 4 of 9) accounting for most of the observed discordance and the wider limits of agreement on the back.

These findings indicate high conditional concordance between HFUS hypoechoicity and μ_s'-identified sites, especially on the chest. However, because HFUS was performed only on μ_s'- identified sites, and HFUS is not a histologic gold standard, these results do not establish diagnostic accuracy of nascent cNF with either modality. The design precludes estimation of negative agreement, intraclass correlation coefficient, or specificity/sensitivity of either method without additional assumptions. To enable symmetric agreement metrics and no–gold-standard accuracy modeling, future studies could incorporate HFUS on a randomized subset of m_s'-negative sites and, where feasible, histologic verification on a subset of sites. Overall, the data indicate that once sites are identified by a lower μ_s', HFUS frequently corroborates these suspected lesions, with only minor shortfalls concentrated in a small number of subjects.

A possible clinical workflow would use wide-field SFDI to screen large anatomical areas (eg, chest, back, extremities) and identify candidate sn_cNF on the basis of m_s' contrast relative to adjacent uninvolved skin. The SFDI acquisition produces an μ_s' map from which automated or semi-automated segmentation can flag focal regions with predefined contrast thresholds (eg, $\mu_s'_{SN} < \mu_s'_{U}$ by a specified margin), generate lesion lists, and provide surface coordinates for coregistration. These candidates are then triaged for targeted HFUS imaging, which serves to verify the hypoechoic phenotype and to quantify lesion geometry, including width, thickness, and depth from the epidermis. When feasible, short sweep volumes can be acquired to estimate cross-sectional area and volume. Coregistered optical and μ_s' images can guide probe placement and ensure reproducible targeting across visits. All measurements are archived to support longitudinal surveillance, with predefined triggers for further evaluation (eg, rapid growth). This staged approach leverages SFDI for rapid, standardized detection across wide fields and employs HFUS for confirmatory characterization, minimizing operator time while providing quantitative metrics suitable for clinical decision making and follow-up.

SFDI reveals decreased optical scattering in cNFs and provides contrast to detect suspected nascent and nearly invisible lesions. Because extracellular matrix, particularly collagen, is a primary factor impacting optical scattering in the skin, the observed differences between cNFs and surrounding uninvolved regions largely reflect differences in collagen microstructure and organization. In cNFs, collagen is composed predominantly of small-diameter fibrils (30–40 nm) (Lassmann et al, 1975), whereas uninvolved skin contains substantially larger-diameter (80–100 nm), more densely packed fibrils (Gross and Schmitt, 1948; Matthew et al, 1987) that efficiently scatter light through both Mie and intermediate-regime scattering mechanisms. In contrast, the thinner fibrils characteristic of cNFs fall closer to the Rayleigh scattering regime, producing lower per-fibril scattering cross-sections and altered angular scattering distribution. At the tissue level, this shift toward finer, disorganized collagen increases the proportion of forward-directed scattering and decreases μ_s' relative to normal skin. Together, these structural differences likely contribute to the weaker scattering phenotype of cNF, impacting imaging contrast, light penetration, and photothermal response during light-based interventions.

Study results may have implications for candidate cNF therapeutic approaches. The ability of SFDI to image and detect both nascent and visible lesions over a large field of view and follow-up with HFUS may allow identifying lesions that could be more responsive to specific therapeutic approaches. Moreover, the hybrid integrated SFDI–HFUS imaging approach introduced in this study can be applied longitudinally to follow and evaluate the effect of candidate therapies (Richey et al, 2024). By identifying cNFs at their earliest, asymptomatic stages, clinicians can intervene proactively, possibly employing effective treatment dosages (radiation or pharmacological) and reduce nonspecific injury to surrounding uninvolved tissue. Early detection can facilitate the potential use of targeted laser or other minimally invasive therapies to slow or possibly prevent the progression of nascent cNFs into larger, disfiguring cNFs, thereby reducing physical discomfort and psychological distress. These potential applications remain exploratory and will require prospective validation.

A limitation of this study is the small number of biopsies collected to confirm that suspected lesions detected by SFDI–HFUS were nascent cNFs. Histopathology remains the definitive gold standard for diagnosing cNFs. Accordingly, this study does not establish diagnostic accuracy or formal performance characteristics of SFDI or HFUS. For ethical and practical reasons, specifically, our intent to monitor nascent lesions longitudinally and avoid unnecessary excisional biopsies in adolescents, we used HFUS as the best available noninvasive surrogate standard in this study. HFUS is widely used in dermatology because it is safe, rapid, and nonionizing and provides high spatial resolution for superficial soft-tissue lesions. Prior studies have shown strong agreement between ultrasound-measured lesion morphology and histopathology across cutaneous neoplasms (Hobayan et al, 2024; Levy et al, 2021; Raffin et al, 2017; Wortsman and Wortsman, 2010), and multiple reports describe characteristic cNF sonographic features such as hypoechogenicity and support HFUS for cNF evaluation (García-Martínez et al, 2023; Oteiza-Rius et al, 2025; Raffin et al, 2017; Thalheimer et al, 2021). Nonetheless, HFUS is not a histologic gold standard and should not replace pathology when a definitive diagnosis is required (eg, suspected malignant transformation or when tissue characterization beyond gross morphology is needed). We will expand our histopathologic

validation in adults where feasible and plan prospectively to target discordant SFDI–HFUS lesions for biopsy in future work to estimate sensitivity and specificity relative to histopathology.

Another limitation of this study is the small number of participants, which includes only those with skin types I–V, despite efforts to recruit patients with all skin types. The limited sample size may not adequately represent the broader NF1 population, potentially overlooking variations in lesion presentation and progression that could occur in a more diverse group. The study may not account for the unique imaging challenges presented by darker skin types (types V–VI), with higher melanin content, which may reduce the contrast between suspected cNF and surrounding uninvolved skin in the μ_s' map. Although the study provides valuable insights into detection of sn_cNF in a subset of the NF1 population, future studies should include a more diverse range of skin types and a larger cohort to ensure that imaging advancements can benefit all patients with NF1.

Study results suggest that decreased optical and acoustic scattering provide useful imaging contrast to identify and characterize sn_cNF lesions that otherwise are not observable with the unaided eye, owing to the overlying dermis that strongly scatters incoming ambient light and obscures these lesions. Despite being classified as 'nascent,' the relatively large lateral extent of some lesions suggests that prior growth may have occurred along directions parallel to the epidermal/dermal interface. Whether these lesions will remain nascent or eventually emerge to raise the air–epidermal interface and become observable to the unaided eye requires further longitudinal imaging and monitoring. Importantly, this study does not establish diagnostic accuracy but rather demonstrates the feasibility of identifying imaging-defined lesion phenotypes suitable for longitudinal observation. Ultimately, the integrated SFDI–HFUS imaging approach may motivate a paradigm shift toward earlier, noninvasive lesion characterization and monitoring, with the potential to inform more effective management of cNFs and improve patient QOL by addressing both medical and cosmetic concerns associated with cNFs.

MATERIALS AND METHODS

Subject enrollment

This prospective exploratory imaging study was conducted in accordance with a protocol approved by the University of California, Irvine Institutional Review Board and adhered to all relevant regulatory standards and the University of California, Irvine's Human Research Protection policies and procedures (protocol number HS#558). Participants were informed about the nature and purpose of the study, and their written, informed consent was obtained before initiating any procedures. For participants aged <18 years, both assent from the minors and informed consent from their parents or legal guardians were obtained before participation. The study was open to individuals diagnosed with NF1, ranging in age from 10 to 80 years, inclusive of all sexes and ethnic groups. Recruitment of subjects was carried out among patients with NF1 under the care of the University of California, Irvine Health system and through collaborative efforts with NF patient advocacy organizations, including the Neurofibromatosis Network (nfnetwork.org) and the Children's Tumor Foundation (ctf.org).

Enrollment occurred consecutively between July 2022 and December 2024, and all eligible patients encountered during this period who consented were enrolled. No a priori power calculation was performed, and the study was designed as a feasibility and pilot evaluation of a wide-field SFDI screening followed by targeted HFUS verification workflow. Accrual was pragmatically limited by the relative infrequency of NF1 and the number of eligible patients presenting during the study period, with an anticipated enrollment of approximately 20 participants over the recruitment window. During this period, 21 consecutive consenting patients were enrolled.

SFDI

SFDI imaging instrumentation and associated analytical methods were described previously (Cuccia et al, 2005). Briefly, SFDI data acquisition involves 2 steps: (i) projecting sinusoidal illumination patterns at different optical wavelengths onto skin using a digital micromirror device and (ii) recording images from the skin of diffusely reflected light for each sinusoidal illumination pattern and optical wavelength (l_i). For each sinusoidal illumination pattern and optical wavelength, the raw diffuse reflectance images are demodulated, and absorption (μ_a) and reduced scattering (μ_s') maps are computed. A commercial SFDI instrument (Reflect RS, Modulim) was utilized for the study (Supplementary Figure S6). This instrument allows measurement of calibrated diffuse reflectance across a field of view measuring 20 × 15 cm^2. The illumination system incorporates 8 light-emitting diodes that project onto the subjects skin, each with 5 sinusoidal illumination line patterns ranging from uniform to 5 line pairs per millimeter at 8 wavelengths ranging from the blue (471 nm) to the near-infrared (851 nm) (Ponticorvo et al, 2014). Depending on the illumination wavelength and the subject's skin pigmentation, camera integration times vary but are generally from 5 to 60 ms. To account for respiratory movements, each skin area was imaged 3 times in succession, discarding any images significantly affected by motion. Completing a full acquisition cycle requires approximately 2 minutes and includes 3 rounds of SFDI image capture.

SFDI generates quantitative maps of the reduced scattering coefficient (μ_s', mm^{-1}) across the imaged field at various wavelengths. We choose a wavelength of 851 nm for the analysis. Measuring μ_s' at 851 nm leverages the near-infrared window where hemoglobin and melanin absorptions are relatively low, yielding a scattering-dominated signal with sufficient penetration depth to detect microstructural perturbations before overt clinical morphology emerges (Phan et al, 2021). The primary outcomes were the site-level mean μ_s' within sn_cNF and within adjacent uninvolved skin and their paired difference. For wide-field screening, these quantitative μ_s' maps were converted to a binary candidate mask (presence/absence of sn_cNF) using a subject- and site-specific contrast threshold relative to the local μ_s' distribution. Binary detections were used to enumerate candidates and guide HFUS targeting.

HFUS imaging

Once an sn_cNF was identified in the SFDI μ_s' map, HFUS was used to examine any anomalous hyposcattering skin areas. HFUS employs higher-frequency sound than conventional ultrasound, typically ranging from 20 to 100 MHz. Shorter acoustic wavelengths of these higher sound frequencies enhance HFUS image resolution, allowing visualization of smaller-sized (~100 mm) subsurface tissue structures. The wireless HFUS probe used in our studies (L20, Clarius) utilizes 128 transceiver elements, each having a pitch of 0.2 mm and a width of 0.15 mm, resulting in an ultrasound aperture of 3.84 mm. The axial resolution of the HFUS probe is approximately

0.1 mm. Image acquisition was set to dermatology mode to record a B-scan (ie, cross-sectional image) with an imaging depth of approximately 5 mm. The B-scan imaging field was configured to 20×5 mm^2, which provided an adequate field of view for assessing cNF lesions. Each sn_cNF was imaged twice, once along the longitudinal (craniocaudal) direction and once along the transverse (left-to-right) direction. Dimensions measured from both images were included in the statistical analysis.

Histological analysis

Three biopsies (visible cNF, sn_cNF, and uninvolved skin) were taken from 3 male subjects (aged 35, 55, and 56 years) and fixed immediately in 10% formalin solution for 24 hours. The fixed tissue underwent standard processing procedures, including dehydration, clearing, and embedding in paraffin. Thin sections were then cut from the paraffin block, mounted onto microscope slides, and subsequently stained using H&E for routine histological analysis.

Imaging procedures and analysis

SFDI images were recorded at 4 skin regions: upper chest, back, and both left and right forearms. During imaging, subjects laid prone or supine on a gurney, with the SFDI imaging head positioned above the imaged skin area. Upon completion of image acquisition for each skin site, data were processed using MI-Analyze software (Modulim) to obtain maps of μ_s' and μ_a at each wavelength (l). Scattering maps were then analyzed using Fiji software (Schindelin et al, 2012) to identify locations of suspected cNF not visible to the unaided eye. This identification was based on the difference in m_s' between the suspected cNF area and surrounding skin sites. First, skin regions with lower μ_s' than surrounding areas at 851 nm wavelengths were identified. Second, if these regions showed minimal or no difference in μ_s' at shorter illumination wavelengths (471 and 526 nm) and color photographs, they were classified as sn_cNF. An example is illustrated in Supplementary Figure S7. Conversely, for visible cNF, the reductions in scattering observed across illumination wavelengths are similar. The scattering map was then coregistered with color digital photographs captured using a Canon G7X camera, facilitated by 4 fiducial marks located at the corners of the SFDI's field of view, along with visible cNF on the skin, using the BigWarp Fiji plugin (Bogovic et al, 2016). Locations of sn_cNF, as identified on the scattering map, were transferred to the color photographs and then marked on the skin for subsequent examination using HFUS imaging.

Prior to HFUS imaging, ultrasound gel was applied to the probe to provide optimal acoustic impedance matching and minimize signal loss. Two HFUS image scan sequences were recorded from each region of interest. The first sequence involved scanning in the caudal direction, providing a longitudinal view of the lesion. The second sequence involved scanning perpendicular to the caudal direction, yielding 2 orthogonal views. This dual-sequence HFUS imaging approach ensured that both longitudinal and transverse planes of the lesions were captured.

Recorded ultrasound B-scan images were analyzed to quantify 3 spatial dimensions of each imaged lesion (Supplementary Figure S8): (i) depth of the lesion, distance from the air–epidermal interface to the most superficial surface of the lesion; (ii) thickness of the lesion, distance from the top to bottom surface of the lesion; and (iii) width of the lesion, width of the lesion at its widest lateral extent. Aspect ratio is calculated by dividing width by thickness.

Statistical analysis

For each subject and site (chest, back), the reduced scattering coefficient (μ_s') at 851 nm was summarized as the mean within sn_cNF (μ_{s_SN}'; averaged across all sn_cNFs present on that site) and the mean within adjacent uninvolved skin (μ_{s_U}'). When a site had no sn_cNF (count = 0), only μ_{s_U}' was recorded; such sites were excluded from paired μ_{s_SN}'–μ_{s_U}' comparisons. Analyses were conducted separately for chest and back and then pooled by concatenating site-level observations (chest + back). The primary comparison tested whether μ_{s_SN}' differed from μ_{s_U}' using a paired-samples *t*-test on within-site differences, reporting the mean difference, 95% CI, *P*-value, and within-subject effect size (Cohen's dz, defined as the mean of the paired differences divided by their standard deviation). Normality of paired differences was examined descriptively; given the magnitude and consistency of effects, the paired *t*-test was robust.

To evaluate trends, we modeled the within-subject contrast $\Delta\mu_s' = \mu_{s_SN}' - \mu_{s_U}'$ at 851 nm as a function of age using simple linear regression, fitted separately by site and in the pooled dataset. Slopes are reported per year, with interpretation per decade. Because 2 sites per subject may introduce mild dependence, pooled regression results are interpreted descriptively; site-specific regressions are not subject to this limitation. We also assessed whether lesion burden related to μ_s' by quantifying monotonic the associations between the number of sn_cNF on a site and either μ_{s_SN}' or μ_{s_U}'. These associations were evaluated using Spearman's rank correlation, separately for chest and back and pooled, given the discrete nature of counts and modest sample size. As secondary covariate analyses, μ_{s_SN}' and μ_{s_U}' were examined against age (continuous), sex, and Fitzpatrick skin type, using Welch's *t*-tests for gender, Spearman correlation for age, and Kruskal–Wallis tests for skin type, emphasizing effect direction in light of small subgroup sizes.

This study used a verification design in which HFUS was performed only on sites identified as sn_cNF by SFDI-derived μ_s' maps. For each subject and body site (chest, back), we recorded the number of sn_cNF sites and, among those, the number with HFUS hypoechoic signal. The primary measure of agreement was the HFUS confirmation rate conditional on μ_s' positivity, p = P(HFUS+ | μ_s' +). We computed site-specific and overall pooled confirmation rates and 95% CIs (Wilson method) using aggregated successes and trials. To compare confirmation between chest and back, we fit a binomial logistic model with a site indicator and trials weights (successes/trials per subject), using subject-level clustering for robust inference; for reporting clarity, we present the ORs for back versus chest with a Wald CI. Because HFUS was only assessed on sn_cNF sites, symmetric agreement measures (intraclass correlation coefficient) are not identifiable and were not used. As complementary descriptions of concordance, we summarized per-subject confirmation proportions (HFUS+/ μ_s' +) among subjects with sn_cNF > 0 and conducted a Bland–Altman analysis on a variance-stabilizing square-root transformation of the counts to estimate mean bias and limits of agreement.

We analyzed sn_cNF lesion thickness across 3 age-defined groups. We conducted a 1-way ANOVA with thickness as the dependent variable and group as the categorical factor with type II sums of squares. ANOVA effect sizes were summarized as eta-squared (η^2) and omega-squared (ω^2). For pairwise contrasts, we used Welch's *t*-tests to accommodate unequal variances and controlled the family-wise error rate using the Holm method. Pairwise effect sizes were calculated as Cohen's d on the basis of the

pooled SD and Hedges' g using the small-sample bias correction. All tests were 2 sided with $\alpha = 0.05$.

Agreement between SFDI-identified candidate sn_cNF counts and HFUS-confirmed lesion counts was assessed at the subject level using Bland–Altman analysis and Lin's concordance correlation coefficient. One paired observation per subject per site (chest or back; n = 21 per site) was included. Because variability tended to increase with lesion count, square-root transformation was applied prior to analysis. Mean bias and 95% limits of agreement were computed separately for chest and back sites.

ETHICS STATEMENT

This study was performed in accordance with the Declaration of Helsinki. This human study was approved by the Institutional Review Board at the University of California, Irvine (approval UCI IRB#558). All parents, guardians, or next of kin provided written informed consent for the minors to participate in this study and for their deidentified photographs to be published in a medical journal. All adult participants provided written informed consent to participate in this study and for their deidentified photographs to be published in a medical journal.

DATA AVAILABILITY STATEMENT

The data are open access and can be found in the neurofibroma data portal hosted on Sage Bionetworks' Synapse platform (https://www.synapse.org/Synapse:syn31619419/datasets/).

ORCIDs

Wangcun Jia: http://orcid.org/0000-0002-5021-3827
Nitesh Katta: http://orcid.org/0000-0001-8097-5489
Gordon T. Kennedy: http://orcid.org/0000-0002-2335-8887
Junsoo Lee: http://orcid.org/0000-0001-8146-6862
Emily Nguyen: http://orcid.org/0009-0009-9682-3805
Oswald Lai: http://orcid.org/0009-0009-7999-1225
Yurie Jeong: http://orcid.org/0009-0008-0804-1495
Rachel Elsanadi: http://orcid.org/0009-0009-5427-2339
James E. Johnson: http://orcid.org/0009-0003-6988-9610
Anat O. Stemmer-Rachamimov: http://orcid.org/0000-0003-3846-5295
J. Stuart Nelson: http://orcid.org/0000-0002-2697-9152
Rafael Sierra: http://orcid.org/0009-0001-2379-0725
Kristen M. Kelly: http://orcid.org/0000-0002-5988-2197
Anthony J. Durkin: http://orcid.org/0000-0001-9124-6388
Thomas E. Milner: http://orcid.org/0000-0002-7532-0004

CONFLICT OF INTEREST

TEM has a financial interest in MasSpec Pen technologies. AJD is a cofounder of Modulim, which makes commercial spatial frequency domain imaging devices. He does not participate in any aspect related to the management of the company. He is in compliance with National Institutes of Health and Baylor College of Medicine policy regarding conflicts of interest.

KMK reports equipment provided by Solta, Syneron/Candela, Thermi RF, Michaelson Diagnostics, Sciton, Lutronic, and Cutera; is a consultant for Shanghai Fudan-Zhangjiang Bio-pharmaceutical, Syneron-Candela, Primus Pharmaceuticals, and Sciton; reports research grants from FDZJ, Lutronic, Michaelson Diagnostics, and Sciton; and reports research supported by American Society for Laser Medicine and Surgery, National Institutes of Health, and Sturge Weber Foundation. The remaining authors state no conflict of interest.

ACKNOWLEDGMENTS

This work was supported by the CDMRP-NFRP (W81XWH2110379 to WJ), DHART SPORE (U54CA196519, Developmental Research Program to TEM), and the Neurofibromatosis Therapeutic Acceleration Program (Biology and Therapeutic Development for Cutaneous Neurofibromas to TEM), The Cancer Prevention and Research Institute of Texas (RR240017 to TEM). We also acknowledge institutional support from the Arnold and Mabel Beckman Foundation and support from the National Institutes of Health, including National Institute of General Medical Sciences grant number R01GM108634 to AJD and GTK, National Center for Research Resources, and the National Center for Advancing Translational Sciences grant number UL1 TR001414. In addition, this material is based, in part, upon technology development supported by the United States Air Force Office of Scientific Research (awards FA9550-20-1-0052 and FA9550-23-1-0685). We would like to thank Hanna Kim and Nicole Wakida, our clinical research coordinators, for their valuable assistance with patient recruitment and study protocol management; Jaishri O. Blakeley, Lu Q. Le, and Sang Y. Lee for their insightful discussion; Andrea Hwang and Kai Zheng from Enterprise Data and Analytics at University of California, Irvine Health; Pamela Flodman; Virginia Kimonis; the Children's Tumor Foundation; and the Neurofibromatosis Network for their assistance with patient recruitment. We also thank Melissa Shive, Neda Zadeh, Tena Rosser, and Samuel Spiegel for referring patients to this study. We sincerely appreciate the patients who participated in this research for their valuable time and commitment. Their support was essential to the success of our research.

Disclaimer

The content is solely the authors' responsibility. Any opinions, findings, and conclusions or recommendations expressed in this material are the authors' and do not necessarily reflect or represent official views of the Neurofibromatosis Therapeutic Acceleration Program, National Institute of General Medical Sciences, National Institutes of Health, United States Air Force, or Department of Defense.

AUTHOR CONTRIBUTIONS

Conceptualization: WJ, NK, RS, KMK, AJD, TEM; Data Curation: WJ, NK; Formal Analysis: WJ, NK, GTK, EN, OL, YJ; Funding Acquisition: WJ, TEM; Investigation: WJ, NK, GTK, JL, EN, OL, YJ, RE, FM, JEJ, AOS-R, KMK; Methodology: WJ, NK, GTK, RS, KMK, AJD, TEM; Writing - Original Draft Preparation: WJ, NK, RS, AJD, TEM; Writing - Review and Editing: WJ, NK, GTK, JL, EN, OL, YJ, RE, FM, JEJ, AOS-R, JSN, RS, KMK, AJD, TEM

DECLARATION OF GENERATIVE ARTIFICIAL INTELLIGENCE (AI) OR LARGE LANGUAGE MODELS (LLMs)

During the preparation of this work, the authors used UCI ZOTGPT for editing to improve grammar, clarity, and readability during manuscript preparation and to generate Python code for statistical analysis. After using this tool, the authors carefully reviewed and edited the content and take full responsibility for the final content.

SUPPLEMENTARY MATERIAL

Supplementary material is linked to the online version of the paper at www.jidonline.org, and at 10.1016/j.jid.2026.02.015.

REFERENCES

Bogovic JA, Hanslovsky P, Wong A, Saalfeld S. Robust registration of calcium images by learned contrast synthesis. In: 2016 IEEE 13th international symposium on biomedical imaging (ISBI). New York: IEEE; 2016. p. 1123–6.

Bromley GS, Sherman JE, Goulian D Jr. Neurofibromatosis-distribution of lesions and surgical treatment. Ann Plast Surg 1982;8:272–6.

Chamseddin BH, Hernandez L, Solorzano D, Vega J, Le LQ. Robust surgical approach for cutaneous neurofibroma in neurofibromatosis type 1. JCI Insight 2019;5:e128881.

Cuccia DJ, Bevilacqua F, Durkin AJ, Tromberg BJ. Modulated imaging: quantitative analysis and tomography of turbid media in the spatial-frequency domain. Opt Lett 2005;30:1354–6.

Duong TA, Bastuji-Garin S, Valeyrie-Allanore L, Sbidian E, Ferkal S, Wolkenstein P. Evolving pattern with age of cutaneous signs in neurofibromatosis type 1: a cross-sectional study of 728 patients. Dermatology 2011;222:269–73.

Durkin AJ, Kim JG, Cuccia DJ. Quantitative near infrared imaging of skin flaps. Frontiers in Biomedical Devices 2008;Vol. 48337:1–2.

Easton DF, Ponder MA, Huson SM, Ponder BA. An analysis of variation in expression of neurofibromatosis (NF) type 1 (NF1): evidence for modifying genes. Am J Hum Genet 1993;53:305–13.

Ehara Y, Yamamoto O, Kosaki K, Yoshida Y. Natural course and characteristics of cutaneous neurofibromas in neurofibromatosis 1. J Dermatol 2018;45:53–7.

Friedman JM. Epidemiology of neurofibromatosis type 1. Am J Med Genet 1999;89:1–6.

García-Martínez FJ, Alfageme F, Duat-Rodríguez A, Andrés Esteban EM, Hernández-Martín A. Clinical and sonographic classification of neurofibromas in children with neurofibromatosis Type 1 - a cluster analysis. Ultraschall Med 2023;44:e118–25.

Gioux S, Mazhar A, Durkin AJ, Tromberg BJ, Cuccia DJ. Special section guest editorial: special section on spatial frequency domain imaging. J Biomed Opt 2019;24:1–2.

Gross J, Schmitt FO. The structure of human skin collagen as studied with the electron microscope. J Exp Med 1948;88:555–68.

Hobayan CGP, Gray AN, Waters MF, Mager LA, Kobayashi S, Essien EW, et al. Diagnostic accuracy of high-frequency ultrasound for cutaneous neoplasms: a narrative review of the literature. Arch Dermatol Res 2024;316:419.

Huson SM, Harper PS, Compston DAS. Von Recklinghausen neurofibromatosis. A clinical and population study in south-east Wales. Brain 1988;111:1355–81.

Jouhilahti EM, Peltonen S, Callens T, Jokinen E, Heape AM, Messiaen L, et al. The development of cutaneous neurofibromas. Am J Pathol 2011;178:500–5505.

Kallionpää RA, Uusitalo E, Leppävirta J, Pöyhönen M, Peltonen S, Peltonen J. Prevalence of neurofibromatosis type 1 in the Finnish population. Genet Med 2018;20:1082–6.

Kennedy GT, Stone R, Kowalczewski AC, Rowland R, Chen JH, Baldado ML, et al. Spatial frequency domain imaging: a quantitative, noninvasive tool for in vivo monitoring of burn wound and skin graft healing. J Biomed Opt 2019;24:1–9.

Kim HJ, Lee KG, Yi SM, Kim JH, Kim IH. Successful treatment of multiple cutaneous neurofibromas using a combination of shave excision and laser photothermocoagulation with a 1,444-nm neodymium-doped yttrium aluminum garnet laser. Dermatol Surg 2012;38:960–3.

Kodra Y, Giustini S, Divona L, Porciello R, Calvieri S, Wolkenstein P, et al. Health-related quality of life in patients with neurofibromatosis Type 1. A survey of 129 Italian patients. Dermatology 2009;218:215–20.

Konecky SD, Mazhar A, Cuccia D, Durkin AJ, Schotland JC, Tromberg BJ. Quantitative optical tomography of sub-surface heterogeneities using spatially modulated structured light. Opt Express 2009;17:14780–90.

Lassmann H, Gebhart W, Stockinger L. The reaction of connective tissue fibers in the tumor of Recklinghausen's disease. Virchows Arch B Cell Pathol 1975;19:167–77.

Lee S, Mey L, Szymanska AF, Takhar HS, Cuccia DJ, Mazhar A, et al. SFDI biomarkers provide a quantitative ulcer risk metric and can be used to predict diabetic foot ulcer onset. J Diabetes Complications 2020;34:107624.

Levy J, Barrett DL, Harris N, Jeong JJ, Yang X, Chen SC. High-frequency ultrasound in clinical dermatology: a review. Ultrasound J 2021;13:24.

Li Y, Blakeley JO, Ly I, Berman Y, Lau J, Wolkenstein P, et al. Current and emerging imaging techniques for neurofibromatosis type 1-associated cutaneous neurofibromas. J Invest Dermatol 2023;143:1397–405.

Lutterodt CG, Mohan A, Kirkpatrick N. The use of electrodessication in the treatment of cutaneous neurofibromatosis: a retrospective patient satisfaction outcome assessment. J Plast Reconstr Aesthet Surg 2016;69:765–9.

Maertens O, Brems H, Vandesompele J, De Raedt T, Heyns I, Rosenbaum T, et al. Comprehensive NF1 screening on cultured Schwann cells from neurofibromas. Hum Mutat 2006;27:1030–40.

Matthew C, Moore MJ, Campbell L. A quantitative ultrastructural study of collagen fibril formation in the healing extensor digitorum longus tendon of the rat. J Hand Surg Br 1987;12:313–20.

Mazhar A, Sharif SA, Cuccia JD, Nelson JS, Kelly KM, Durkin AJ. Spatial frequency domain imaging of port wine stain biochemical composition in response to laser therapy: a pilot study. Lasers Surg Med 2012;44:611–21.

Méni C, Sbidian E, Moreno JC, Lafaye S, Buffard V, Goldzal S, et al. Treatment of neurofibromas with a carbon dioxide laser: a retrospective cross-sectional study of 106 patients. Dermatology 2015;230:263–8.

Muir D, Neubauer D, Lim IT, Yachnis AT, Wallace MR. Tumorigenic properties of neurofibromin-deficient neurofibroma schwann cells. Am J Pathol 2001;158:501–13.

Nagrani NS, Bhawan J. Histopathological variants of cutaneous neurofibroma: a compendious review. Dermatopathology (Basel) 2022 Dec 26;10:1–19.

Nguyen JQ, Crouzet C, Mai T, Riola K, Uchitel D, Liaw LH, et al. Spatial frequency domain imaging of burn wounds in a preclinical model of graded burn severity. J Biomed Opt 2013;18:66010.

Oteiza-Rius I, Estenaga Pérez de Albéniz Á, Hernández-Martin Á, Alfageme Roldán F, García-Martínez FJ. Sonographic characterization of red-blue neurofibromas in patients with neurofibromatosis type 1: an observational prospective study. J Ultrasound Med 2025;44:703–9.

Page PZ, Page GP, Ecosse E, Korf BR, Leplege A, Wolkenstein P. Impact of neurofibromatosis 1 on quality of life: a cross-sectional study of 176 American cases. Am J Med Genet A 2006;140:1893–8.

Peltonen J, Jaakkola S, Lebwohl M, Renvall S, Risteli L, Virtanen I, et al. Cellular differentiation and expression of matrix genes in Type-1 neurofibromatosis. Lab Invest 1988;59:760–71.

Phan T, Rowland R, Ponticorvo A, Le BC, Wilson RH, Sharif SA, et al. Characterizing reduced scattering coefficient of normal human skin across different anatomic locations and Fitzpatrick skin types using spatial frequency domain imaging. J Biomed Opt 2021;26:026001.

Ponticorvo A, Burmeister DM, Yang B, Choi B, Christy RJ, Durkin AJ. Quantitative assessment of graded burn wounds in a porcine model using spatial frequency domain imaging (SFDI) and laser speckle imaging (LSI). Biomed Opt Express 2014;5:3467–81.

Ponticorvo A, Taydas E, Mazhar A, Scholz T, Kim HS, Rimler J, et al. Quantitative assessment of partial vascular occlusions in a swine pedicle flap model using spatial frequency domain imaging. Biomed Opt Express 2013;4:298–306.

Raffin D, Zaragoza J, Georgescou G, Mourtada Y, Maruani A, Ossant F, et al. High-frequency ultrasound imaging for cutaneous neurofibroma in patients with neurofibromatosis type I. Eur J Dermatol 2017;27:260–5.

Richey P, Funk M, Sakamoto F, Plotkin S, Ly I, Jordan J, et al. Noninvasive treatment of cutaneous neurofibromas (cNFs): results of a randomized prospective, direct comparison of four methods. J Am Acad Dermatol 2024;90:767–74.

Roenigk RK, Ratz JL. CO_2 laser treatment of cutaneous neurofibromas. J Dermatol Surg Oncol 1987;13:187–90.

Saidian M, Lakey JRT, Ponticorvo A, Rowland R, Baldado M, Williams J, et al. Characterisation of impaired wound healing in a preclinical model of induced diabetes using wide-field imaging and conventional immunohistochemistry assays. Int Wound J 2019;16:144–52.

Schindelin J, Arganda-Carreras I, Frise E, Kaynig V, Longair M, Pietzsch T, et al. Fiji: an open-source platform for biological-image analysis. Nat Methods 2012;9:676–82.

Serra E, Puig S, Otero D, Gaona A, Kruyer H, Ars E, et al. Confirmation of a double-hit model for the NF1 gene in benign neurofibromas. Am J Hum Genet 1997;61:512–9.

Thalheimer RD, Merker VL, Ly KI, Champlain A, Sawaya J, Askenazi NL, et al. Validating techniques for measurement of cutaneous neurofibromas: recommendations for clinical trials. Neurology 2021;97:S32–41.

Wolkenstein P, Zeller J, Revuz J, Ecosse E, Leplège A. Quality-of-life impairment in neurofibromatosis type 1: a cross-sectional study of 128 cases. Arch Dermatol 2001;137:1421–5.

Wortsman X, Wortsman J. Clinical usefulness of variable-frequency ultrasound in localized lesions of the skin. J Am Acad Dermatol 2010;62:247–56.

Zarchi K, Wortsman X, Jemec GB. Ultrasound as a diagnostic aid in identifying neurofibromas. Pediatr Dermatol 2014;31:535–7.

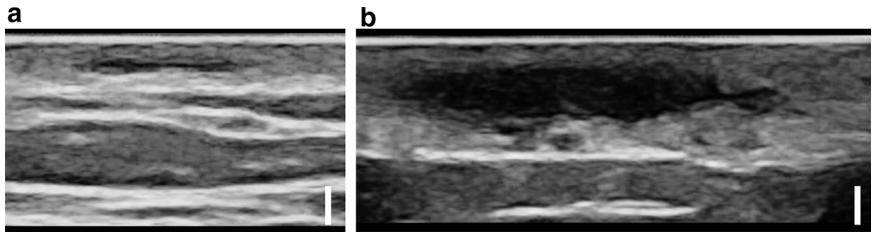

Supplementary Figure S1. HFUS cross-sectional images of cNF of different geometries. (**a**) A thin cNF with a width of 3.9 mm and a thickness of 0.4 mm located 0.7 mm beneath the skin surface. (**b**) A large cNF with a width of 11.2 mm and a thickness of 2.3 mm located 0.5 mm beneath the skin surface. Bar = 1 mm. cNF, cutaneous neurofibroma; HFUS, high-frequency ultrasound.

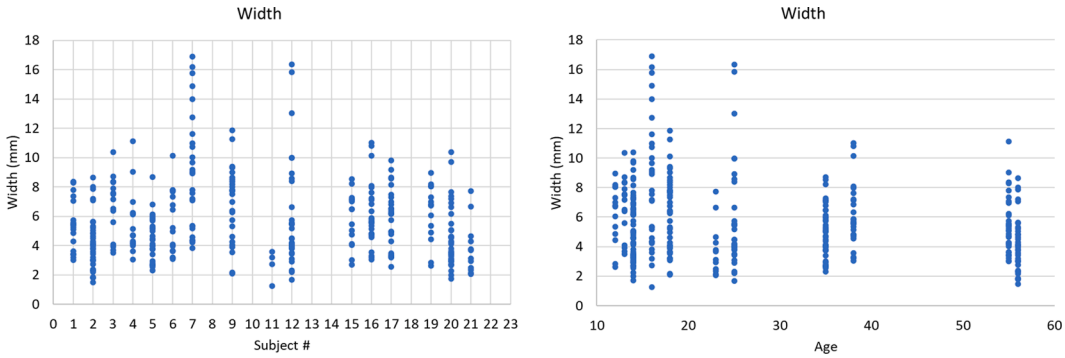

Supplementary Figure S2. Width of the sn_cNF measured from HFUS cross-sectional images for all subjects. HFUS, high-frequency ultrasound; sn_cNF, suspected nascent cutaneous neurofibroma.

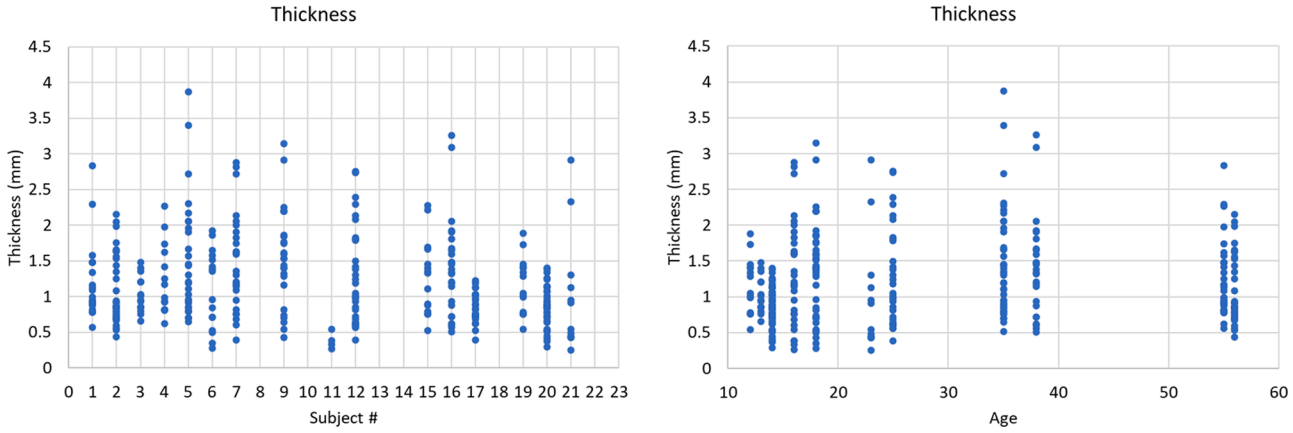

Supplementary Figure S3. Thickness of the sn_cNF measured from HFUS cross-sectional images for all subjects. HFUS, high-frequency ultrasound; sn_cNF, suspected nascent cutaneous neurofibroma.

Supplementary Figure S4. Depth of the sn_cNF measured from HFUS cross-sectional images for all subjects. HFUS, high-frequency ultrasound; sn_cNF, suspected nascent cutaneous neurofibroma.

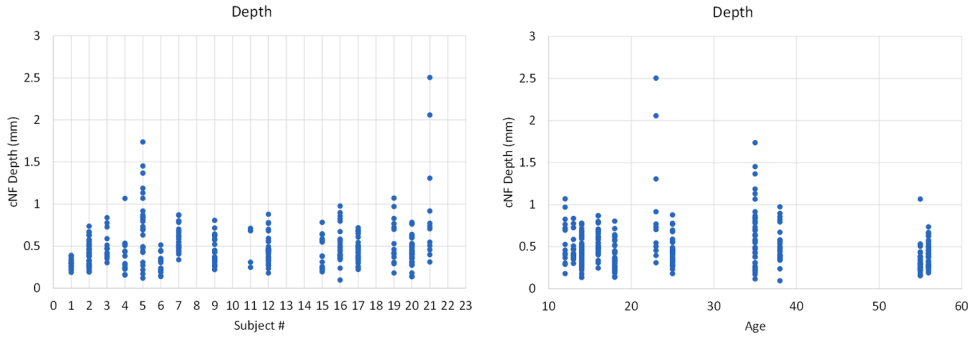

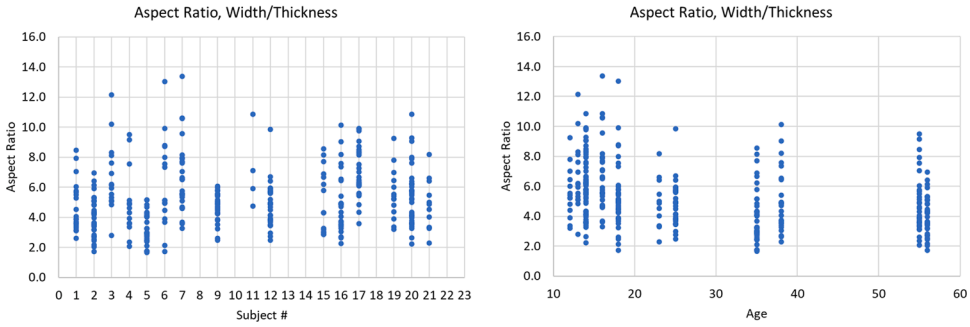

Supplementary Figure S5. Aspect ratio of the sn_cNF measured from HFUS cross-sectional images for all subjects. HFUS, high-frequency ultrasound; sn_cNF, suspected nascent cutaneous neurofibroma.

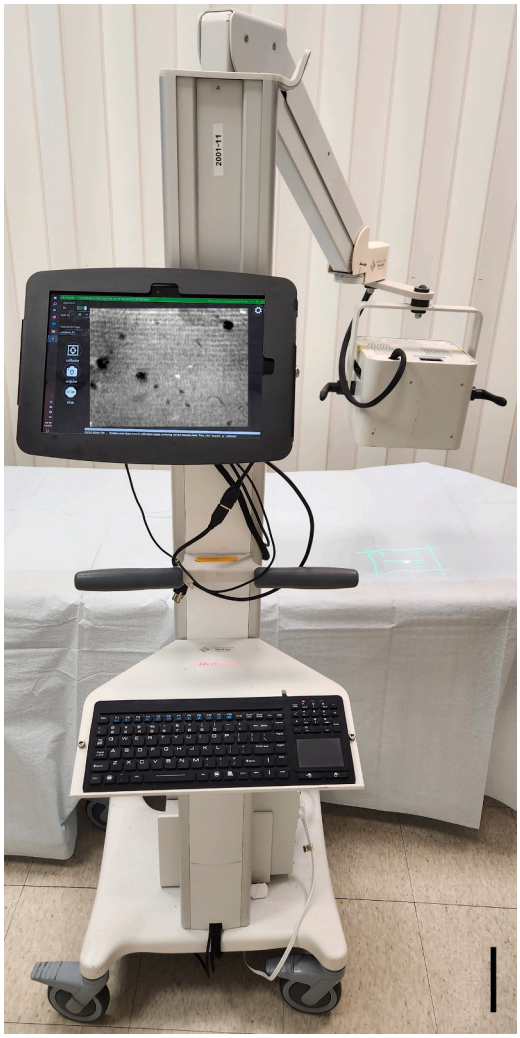

Supplementary Figure S6. Cart-based SFDI instrument (Reflect RS, Modulim) utilized to record diffuse reflectance images and compute μ_s' and μ_a. Bar = 100 mm. SFDI, spatial frequency domain imaging.

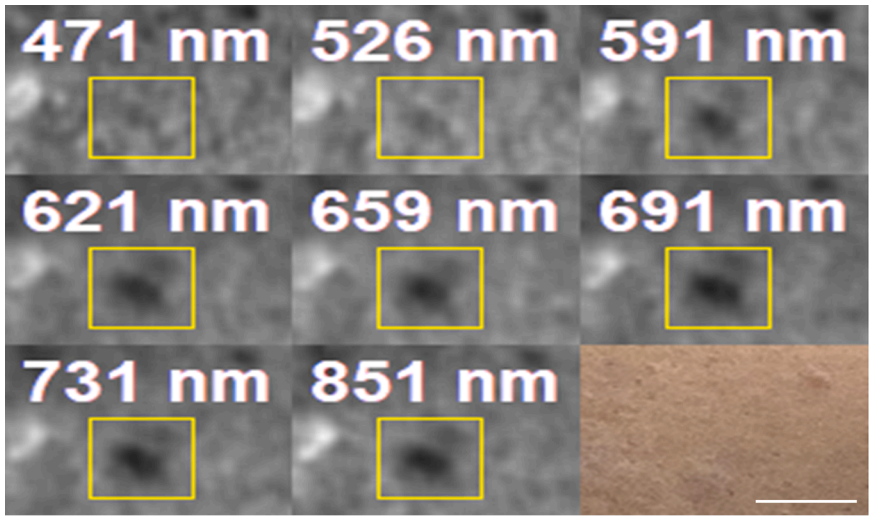

Supplementary Figure S7. Scattering maps across 8 wavelengths and a color photo of a sn_cNF. The sn_cNF region, highlighted within the yellow box, shows a lower μ_s' at longer wavelengths. Bar = 10 mm. sn_cNF, suspected nascent cutaneous neurofibroma.

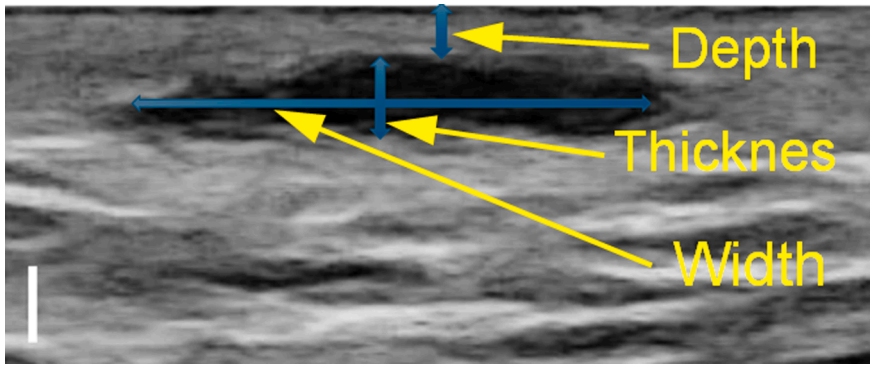

Supplementary Figure S8. Quantification of a sn_cNF in HFUS cross-sectional image. Bar = 1 mm. HFUS, high-frequency ultrasound; sn_cNF, suspected nascent cutaneous neurofibroma.

Supplementary Table S1. Characteristics of sn_cNF on the Left Arm and Visible cNF on Chest, Back, and Left and Right Arms

	Nascent cF			sN_cNF		Visible cNF								
Subject ID	Age, y	Sex	Skin Type	Left arm	μ_s', SN/U[1]	Chest	μ_s', V/U[1]	Back	μ_s', V/U[1]	Left arm	μ_s', V/U[1]	Right arm	μ_s', V/U[1]	Total
3	11	F	III	0		1	1.14/1.44	0	/1.52	1	0.95/1.33	0	/1.58	2
19	12	M	III	0		0	/1.49	0	/1.47	0	/1.48	0	/1.46	0
17	13	M	I	0		1	1.30/1.63	2	1.40/1.69	0	/1.71	1	1.45/1.62	4
7	14	M	II	1	1.39/1.58	0	/1.71	3	1.36/1.56	0	/1.58	0	/1.57	3
20	14	M	III	0		3	1.30/1.66	7	1.22/1.55	1	1.19/1.63	3	1.36/1.46	14
8	15	M	III	0		0	/1.69	0	/1.52	0	/1.72	0	/1.63	0
11	15	M	IV	0		0	/1.62	0	/1.65	0	/1.61	0	/1.63	0
9	17	M	IV	0		0	/1.38	7	1.01/1.37	0	/1.55	1	1.44/1.61	8
10	17	M	II	0		0	/1.90	0	/1.77	0	/1.85	0	/1.82	0
6	18	F	I	0		1	1.13/1.37	1	/1.32	0	/1.47	2	1.20/1.37	4
21	23	F	III	2	1.09/1.33	4	0.95/1.19	1	0.92/1.19	0	/1.33	0	/1.23	5
12	24	M	I	0		2	1.27/1.50	3	1.15/1.40	0	/1.54	0	/1.52	5
13	29	M	I	0		0	/1.60	0	/1.67	0	/1.74	0	/1.66	0
18	30	F	II	0		0	/1.20	0	/1.18	0	/1.35	0	/1.31	0
5	35	M	IV	0		7	1.26/1.43	9	1.01/1.36	4	1.08/1.50	1	1.16/1.46	21
15	35	F	IV	1	1.21/1.32	1	0.91/1.25	1	1.09/1.31	1	1.17/1.32	1	1.00/1.20	4
16	37	F	IV	0		18	0.95/1.24	11	1.01/1.31	3	1.04/1.43	5	1.04/1.31	37
1	55	F	II	0		205	0.83[1]/1.19	67	0.95[1]/1.21	18	0.96[1]/1.32	29	0.92[1]/1.27	319
4	55	M	II	0		131	0.90[1]/1.23	89	1.04[1]/1.38	20	1.07[1]/1.36	11	1.14[1]/1.41	251
2	56	M	II	0		10	0.96[1]/1.23	11	0.95[1]/1.25	9	1.18/1.37	8	1.31/1.46	38
14	62	F	V	0		91	1.0[1]/1.38	199	0.99[1]/1.26	69	0.94[1]/1.31	55	0.98[1]/1.31	414

Abbreviations: cNF, cutaneous neurofibroma; F, female; ID, identification; M, male; sn_cNF, suspected nascent cutaneous neurofibroma.
[1]Measurements were an average of 10 cNFs.

Supplementary Table S2. Statistics of Reduced Scattering Coefficient (μ_s') for sn_cNF and Uninvolved Skin at 851 nm Wavelength

				Reduced Scattering Coefficient, μ_s' (mm^{-1})					
Statistic	Age, y	Subject Count	Pairs	sn_cNF	Uninvolved	Difference	*t*-test *P*-Value	95% CI	Effect size Cohen's dz
Chest									
Group_I	10–19	10	8	1.30 ± 0.15	1.54 ± 0.13	−0.24	.000	−0.30 to −0.17	−2.97
Group_II	20–49	7	4	1.16 ± 0.14	1.33 ± 0.16	−0.17	.006	−0.25 to −0.09	−3.52
Group_III	≥50	4	2	1.00 ± 0.00	1.27 ± 0.05	−0.27	.084	−0.71 to 0.18	−5.35
All		21	14	1.22 ± 0.17	1.44 ± 0.17	−0.22	.000	[−0.26 to −0.18	−3.02
Back									
Group_I	10–19	10	7	1.29 ± 0.13	1.48 ± 0.10	−0.2	0	−0.24 to −0.16	−4.46
Group_II	20–49	7	4	1.18 ± 0.03	1.35 ± 0.04	−0.16	.007	−0.24 to −0.09	−3.35
Group_III	≥50	4	2	1.05 ± 0.03	1.23 ± 0.03	−0.18	0	NA–NA	NA
All		21	13	1.22 ± 0.13	1.40 ± 0.13	−0.18	0	−0.21 to −0.16	−4.28
Both chest and back									
Group_I	10–19	10	15	1.29 ± 0.14	1.51 ± 0.12	−0.22	0	−0.26 to −0.18	−3.3
Group_II	20–49	7	8	1.17 ± 0.10	1.34 ± 0.11	−0.17	0	−0.20 to −0.13	−3.69
Group_III	≥50	4	4	1.03 ± 0.03	1.25 ± 0.04	−0.22	.004	−0.31 to −0.13	−3.92
All		21	27	1.22 ± 0.15	1.42 ± 0.15	−0.2	0	−0.23 to −0.18	−3.26

Abbreviations: CI, confidence interval; NA, not available; sn_cNF, suspected nascent cutaneous neurofibroma.

Supplementary Table S3. Agreement between SFDI-Identified Candidate sn_cNF Counts and HFUS-Confirmed Lesions

Site	n (Pairs)	CCC	Pearson r	Mean Bias	SD of Differences	Lower LoA	Upper LoA	Transform
Chest	21	0.993	0.994	0.03	0.09	−0.15	0.20	Square-root
Back	21	0.920	0.932	0.06	0.22	−0.38	0.49	Square-root

Abbreviations: CCC, concordance correlation coefficient; HFUS, high-frequency ultrasound; LoA, limit of agreement; SFDI, spatial frequency domain imaging; sn_cNF, suspected nascent cutaneous neurofibroma.

Agreement statistics were computed on square-root–transformed lesion counts to stabilize variance prior to Bland–Altman analysis. CCC denotes Lin's CCC. LoA indicates 95% LoAs.

Supplementary Table S4. Geometrical Characteristics of sn_cNF Derived from HFUS Cross-Sectional Images

Statistic	Age, y	Subject Count	sn_cNF Count	Width, mm			Thickness, mm			Depth, mm			Aspect Ratio, Width/Thickness		
				Mean ± SD	Min	Max	Mean ± SD	Min	Max	Mean ± SD	Min	Max	Mean ± SD	Min	Max
Group_I	10–19	10	53	5.45 ± 2.29	1.3	11.9	1.00 ± 0.43	0.3	2.25	0.47 ± 0.19	0.1	1.07	5.72 ± 2.01	2.2	13
Group_II	20–49	7	40	4.55 ± 1.81	1.7	9.98	1.09 ± 0.49	0.3	2.39	0.65 ± 0.42	0.1	2.5	4.59 ± 1.76	1.7	9.86
Group_III	≥50	4	19	4.81 ± 1.67	1.8	8.9	1.21 ± 0.49	0.4	2.15	0.43 ± 0.20	0.2	0.88	4.30 ± 1.44	2.2	8.03
All		21	112	5.02 ± 2.01	1.3	11.9	1.07 ± 0.46	0.3	2.39	0.52 ± 0.30	0.1	2.5	5.08 ± 1.86	1.7	13

Abbreviations: HFUS, high-frequency ultrasound; Max, maximum; Min, minimum; sn_cNF, suspected nascent cutaneous neurofibroma.

Supplementary Table S5. Statistical Analysis of sn_cNF Thickness across Age Groups: 1-Way ANOVA for Lesion Thickness by Age Group

Statistic	Value
F (2, 218)	3.13
P-value	.046
η^2	0.028
ω^2	0.019

Abbreviation: sn_cNF, suspected nascent cutaneous neurofibroma.

One-way ANOVA indicated a statistically significant overall group effect with small effect sizes. After Holm correction, none of the pairwise comparisons remained statistically significant.

Supplementary Table S6. Statistical Analysis of sn_cNF Thickness across Age Groups: Pairwise Comparisons (Welch's *t*-Tests, Holm Adjusted)

Comparison	Mean Difference (mm)	Holm-Adjusted *P*-Value	Raw *P*-Value
Group I versus group II	−0.09	.348	.174
Group I versus group III	−0.21	.071	.024
Group II versus group III	−0.11	.348	.249

Abbreviation: sn_cNF, suspected nascent cutaneous neurofibroma.

One-way ANOVA indicated a statistically significant overall group effect with small effect sizes. After Holm correction, none of the pairwise comparisons remained statistically significant.